Available online at www.sciencedirect.com
ScienceDirect
Trans. Nonferrous Met. Soc. China 28(2018) 2199−2213
Transactions of Nonferrous Metals Society of China
www.tnmsc.cn

Microstructure characterization and effect of extrusion temperature on biodegradation behavior of Mg−5Zn−1Y−*x*Ca alloy

F. DOOST MOHAMMADI, H. JAFARI

Materials Engineering Department, Faculty of Materials Engineering and Modern Technologies, Shahid Rajaee Teacher Training University, 16785-136 Tehran, Iran

Received 24 November 2017; accepted 16 April 2018

Abstract: Microstructure and biodegradation behavior of as-cast and hot extruded Mg−5Zn−1Y alloy containing different amounts of calcium (0.0%, 0.1%, 0.5%, and 1.0%, mass fraction) were explored. The extrusion process was conducted at three different temperatures of 300, 330, and 370 °C. Chemical composition, phase constitution, microstructure, and biodegradation behavior of the alloys were investigated. The macro- and micro-scopic examination revealed that the addition of Ca refines the grain structure and forms an intermetallic phase, $Ca_2Mg_6Zn_3$. The hot extrusion process resulted in breaking the intermetallic phases into fine particles routed to the extrusion direction. Moreover, dynamic recrystallization happened in almost all alloys, and more bimodal microstructure was formed in the alloys when the alloys were extruded at 370 °C. Polarization curves showed no passive region, which indicated that active polarization dominated in the alloys; therefore, grain refining through Ca addition and dynamic recrystallization over hot extrusion operation increased biodegradation rate. The results show that the as-cast Mg−5Zn−1Y−0.1Ca alloy provides the highest corrosion resistance, and the extruded Mg−5Zn−1Y−0.5Ca alloy at 300 °C shows the lowest biodegradation rate among the extruded alloys. Therefore, hot extrusion does not always improve the biodegradation behavior of magnesium alloys.

Key words: magnesium alloys; extrusion temperature; biodegradation; recrystallization; bimodal microstructure

1 Introduction

Magnesium (Mg) and its alloy, due to their close density and mechanical properties to those of the bone [1], as well as the biocompatibility, biodegradability, and non-toxicity in the human body [2,3], are considered as the new generation and suitable alternative orthopedic biodegradable materials for the commercial biomaterials such as stainless steel, titanium and its alloys, cobalt−chromium alloys [4]. In addition, the long-term use of Mg alloys in the body does not cause any side effects such as allergic reactions and sensitivity [5]. However, the major limitation of these alloys is the low corrosion resistance in the human body which reduces the mechanical integrity of the implant before the bone is fully healed [6]. Various techniques like alloying [7], heat treating [8], mechanical working [9,10], and surface modification and coating [11] have been tried to control the corrosion rate of such materials. In general, aluminum (Al), zinc (Zn), manganese (Mn), calcium (Ca), yttrium (Y), zirconium (Zr), and rare earth (RE) are common alloying elements to improve physical and mechanical properties of Mg. Alloying elements must carefully be chosen to maintain the biocompatibility of Mg in biomedical applications. For instance, Al as the main alloying elements to boost the strength and corrosion resistance of Mg-based alloys decreases phosphate in tissue and reduces its absorption in the digestive system, resulting in a gradual decline of wits, leading to toxification of living cells if the concentration exceeds the permissible level [12,13]. Alloying not only significantly reduces the risk of toxicity but develops biodegradability and biocompatibility of Mg. Zn [14] and Ca [15] are two essential elements in the human body which improve the mechanical strength and corrosion resistance of Mg. Also, their existence does not cause cytotoxicity in the body [16]. Considering Ca as the main component of bone, its usage in Mg implant accelerates bone growth. On the other hand, simultaneous release of Mg^{2+} and Ca^{2+} ions from the implant material benefits bone healing [14,17]. Y improves technological characteristics, such as casting [18] and ductility [19], and enhances mechanical

Corresponding author: H. JAFARI; Tel: +98-9120927517; Fax: +98-21-22970022; E-mail: hjafari@sru.ac.ir
DOI: 10.1016/S1003-6326(18)64865-4

and corrosion properties of Mg alloys [20,21].

Wrought Mg components are usually shaped by hot working processes, including extrusion, rolling, forging and even deep drawing in the temperature range of 250−450 °C under no protective atmosphere [22]. In general, hot-worked components, due to their fine-grained and nonporous microstructure, possess more superior mechanical properties than castings [23]. ZHANG et al [24] investigated the effect of Y on the corrosion behavior of the extruded Mg−Y alloy and reported that an increase in Y content refines microstructure especially after the extrusion, leading to a decreased corrosion resistance. ZENG et al [25] studied the microstructure and corrosion behavior of extruded Mg−Ca alloy. They found that although increasing Ca content refines the grains and produces an improved corrosion resistance, it increases the volume fraction of Mg_2Ca cathode area, resulting in accelerated corrosion of α-Mg matrix through galvanic effect. They also reported that in order to keep good corrosion resistance of Mg−Ca alloy, the addition of Ca is preferred to be less than 1%. This might be a guideline for the design of Ca-containing Mg alloys having good corrosion resistance. SUN et al [19] studied the effect of extrusion temperature on the microstructure and mechanical properties of Mg−3.0Zn−0.2Ca−0.5Y alloy. Increased dynamic recrystallized (DRX) grains under the increased extrusion temperature was reported. HOU et al [26] and GUI et al [27] investigated the microstructure and corrosion behavior of extruded Mg−3Sn−1Zn−0.5Mn and Mg−3.0Gd−2.7Zn−0.4Zr−0.1Mn alloys in simulated body fluid (SBF), respectively at a fixed temperature and extrusion rate. They reported that extrusion process causes microstructure refinement, leading to a positive effect on the corrosion resistance of the alloys. BEAK et al [28] investigated the effect of 0.1% and 0.5% Ca on microstructure and corrosion properties of AZ61 alloy extruded at 300 °C with the extrusion ratio of 1:30. TONG et al [29] studied the effect of cerium (Ce) and lanthanum (La) addition on microstructure and corrosion behavior of Mg−5.3Zn−0.6Ca alloy extruded at 300 °C. They showed that alloying process results in the formation of secondary phases with higher electrochemical potentials (cathode) compared to α-Mg (anode). The secondary phases are broken during the extrusion and develop more microgalvanic cell, leading to a decreased corrosion resistance. There are also some studies reporting the improved effects of extrusion on corrosion behavior of Mg alloys [26,27]. It is also believed that mechanical working does not always improve the corrosion resistance of Mg alloys [28,29]. Therefore, it is worth to investigate the effect of extrusion process on the corrosion behavior of biodegradable Mg alloys. To the authors' knowledge, no research may be found to investigate the effect of extrusion temperature on corrosion behavior of ternary or quaternary Mg alloys in SBF. In addition, there are discrepancies in reports regarding the corrosion behavior of extruded Mg alloy. In this work, therefore, to attain the advantages of alloying elements as well as the extrusion process, the effect of 0−1.0% Ca and different extrusion temperatures, on the corrosion behavior of Mg−5Zn−1Y alloy in SBF are investigated.

2 Experimental

2.1 Alloy preparation, extrusion process and sample preparation

In order to prepare $Mg_{94-x}Zn_5Y_1Ca_x$ alloys, commercially pure Mg (99.95%), Zn (99.75%), and Ca (99.90%) ingots, and Mg−30Y master alloy (Table 1) were first melted in a graphite crucible at 750 °C using an induction furnace. The melted alloys were then cast into a simple cylindrical steel mold, with a diameter of 30 mm and height of 130 mm, preheated to 200 °C. Due to the high affinity of Mg to oxygen, all melting stages, including heating, alloying and casting were conducted under a shield of high purity argon gas. The cast alloys were analyzed by inductively coupled plasma optical emission spectrometry (ICP-OES, Varian VISTA-PRO with a quartz torch) to ensure achieving the required chemical composition. They were then heated at 385 °C for 18 h, followed by quenching in warm water with 40 °C to prepare homogenized materials for the extrusion process. Afterward, the homogenized samples were extruded at three different temperatures of 300, 330, and 370 °C with a fixed extrusion ratio of 1:6, and a constant displacement speed of 1 mm/s. The extruded samples were left to cool to ambient temperature in air.

Table 1 Chemical composition of Mg−30Y master alloy (mass fraction, %)

Y	Fe	Ni	Cu	Si	Al	Zn	Mn	Mg
29.840	0.019	0.002	0.003	0.006	0.005	0.004	0.006	Bal.

2.2 Microstructure characterization

Specimens were cut from the as-cast and extruded samples to characterize the microstructure. The specimens were ground with SiC papers up to a final 5000 grit, then polished using diamond paste followed by etching using Picral solution (1 g picric acid + 2.5 mL acetic acid + 2.5 mL H_2O + 17 mL ethanol) for 20 s. An optical microscope (OM, Carl Zeiss Jena), a scanning electron microscope (SEM, Tescan, MIRA3) equipped with an energy dispersive X-ray spectroscopy (EDS) device, and X-ray diffraction (XRD, Unisantis) technique were utilized for the characterization. Macroscopic images were also prepared to reveal grain structure and

to compare grain size of alloys after the sample preparation, and etching with Picral etchant (2 g picric acid + 5 mL acetic acid + 5 mL H_2O + 25 mL ethanol) for 10 s. The average grain size of the samples was determined using the linear intercept procedure according to the standard ASTM E112-13.

2.3 Biodegradation assessment

Electrochemical polarization and immersion tests were performed to assess the in-vitro biodegradation behavior of the as-cast and extruded samples in simulated body fluid (SBF) with the chemical composition of 8.035 g/L NaCl, 0.355 g/L $NaHCO_3$, 0.225 g/L KCl, 0.231 g/L $K_2HPO_4.3H_2O$, 0.311 g/L $MgCl_2·6H_2O$, 0.292 g/L $CaCl_2$, 0.072 g/L Na_2SO_4, 39 mL of 1 mol/L HCl and 6.118 g/L $(CH_2OH)_3CNH_2$ [30]. pH of the SBF was adjusted to 7.4 using a pH meter (SANA SL−901). For the polarization test, a potentiostat/galvanostat apparatus (BHP 2064) connected to a PC with a scan rate of 1 mV/s started from −2.5 to −1 V was used. Specimens sized 10 mm × 10 mm were cut from the as-cast and extruded (parallel to the extrusion direction) samples, ground with SiC papers up to a final 2500 grit, washed with distilled water and dried using blowing hot. A standard cell that consists of a working electrode (the prepared specimens), a saturated calomel reference electrode (SCE), and a counter electrode (platinum electrode), containing 50 mL SBF at 37 °C was used to perform the experiment and plot the corresponding polarization curves. Corrosion rate (P_i, mm/a) of the specimens was calculated by Eq. (1) [8] using corrosion current density (J_{corr}, A/cm^2) extracted from the curves.

$$P_i=2.285\times10^4\times J_{corr} \quad (1)$$

Immersion test was carried out according to ASTM NACE / ASTM G31-12a. Specimens with the diameter and length of 10 mm were cut from the as-cast and extruded samples and prepared according to the procedure explained above for the electrochemical test. The specimens were weighed with a digital scale, having an accuracy of ±0.0001, then immersed in a beaker containing 200 mL SBF for 168 h. They were removed from the SBF in an interval of 24 h, soaked in a solution composed of 180 g/L chromium trioxide, 10 g/L silver nitrate and 20 g/L barium nitrate for 2 min to remove the corrosion products, then rinsed and dried, and weighed again. Before the specimens were re-immersed, pH of the SBF was measured using the pH meter. With the aid of Eq. (2), the corrosion rate (P_w, mm/a) corresponding to the immersion test was calculated. In Eq. (2), m is the mass loss (mg), D is the density of alloy (g/cm^3), A is the surface area of the specimens (cm^2), and t is the immersion time (h). Both electrochemical polarization and immersion tests were repeated for two and three times, respectively, to obtain and report the reliable results.

$$P_w=\frac{87.6\ m}{DAt} \quad (2)$$

3 Results and discussion

3.1 Chemical composition of alloys

Table 2 presents chemical composition of the investigated alloys, suggesting the ZW51 nomination for the alloys having different Ca contents. It also supports the nominal composition of the alloys, revealing appropriate procedures for the alloying, processing and casting of the molten metal for the fabrication of the investigated alloys.

3.2 Microstructure characterization of as-cast, homogenized and extruded alloys

Figure 1 shows typical macroscopic images of the as-cast alloys. It can be clearly seen that increasing Ca content causes more refined microstructure alloy. It is interesting to note that the ability of each alloying element to refine the microstructure can be found through growth restriction factor (GRF); the higher the GRF, the more the refined microstructure. Compared to GRF of the common alloying elements like Sn (9.25), Zn (5.31), Al (4.32), Y (1.70), and etc, Ca has a high amount of GRF (11.91) and it successfully refines grains of magnesium alloy [31]. In addition, the formation of a constitutional undercooling at an area immediately adjacent to the solid/liquid interface results in grain growth confinement [32]. On the other hand, increasing the number of alloying elements in an alloy reduces the

Table 2 Chemical composition of Mg−5Zn−1Y−xCa alloys (x= 0.0, 0.1, 0.5, and 1.0)

Alloy	Mass fraction/%								
	Zn	Y	Ca	Fe	Mn	Al	Cu	Si	Mg
Mg−5Zn−1Y	4.931	0.923	0.003	0.003	0.005	0.057	0.008	0.018	Bal.
Mg−5Zn−1Y−0.1Ca	4.698	0.815	0.089	0.003	0.005	0.058	0.008	0.010	Bal.
Mg−5Zn−1Y−0.5Ca	4.632	0.893	0.532	0.003	0.005	0.073	0.008	0.002	Bal.
Mg−5Zn−1Y−1Ca	4.549	0.908	1.036	0.003	0.005	0.066	0.008	0.006	Bal.

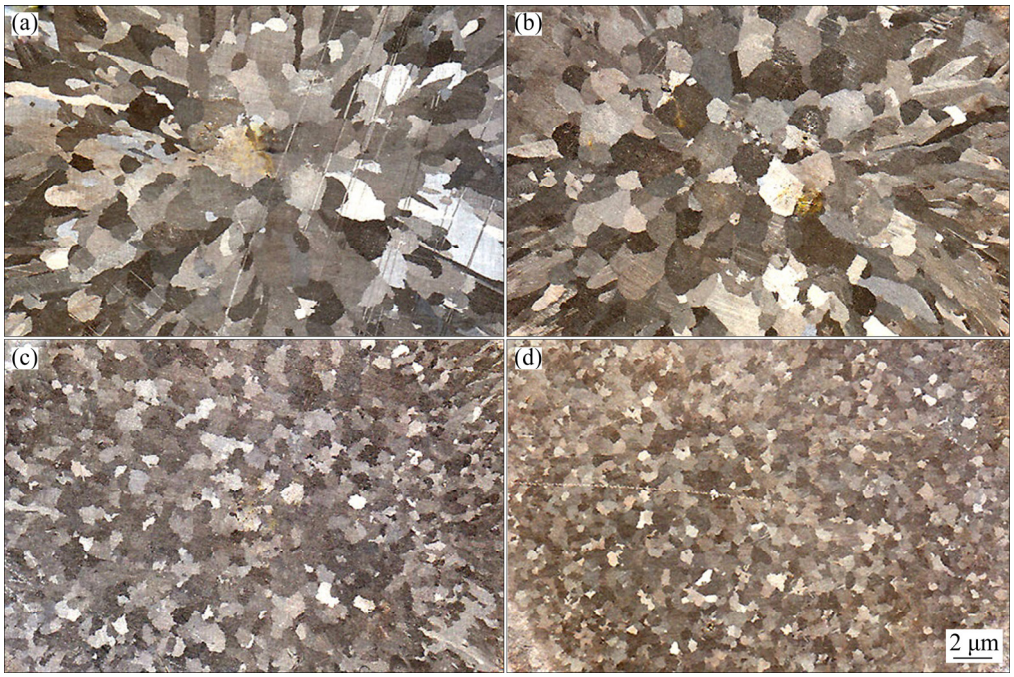

Fig. 1 Typical macroscopic images of as-cast Mg−5Zn−1Y−*x*Ca alloys: (a) *x*=0; (b) *x*=0.1; (c) *x*=0.5; (d) *x*=1.0

solubility of the elements into matrix compared to the binary alloy. It is more probably a low variation in grain size can be seen in a low Ca content alloy.

Figure 2 represents the typical OM images of the Mg−5Zn−1Y alloy having different Ca contents. The images reveal that the cast alloys are composed of a fully-equiaxed dendritic structure, confirming the high cooling rate and non-equilibrium solidification. Moreover, the presence of black areas embedded in the matrix suggests a limited solution of the alloying elements in Mg. Furthermore, the higher the content of Ca, the finer and the more the continuity precipitations and the higher their amounts.

Figure 3 shows the SEM images of the Mg−5Zn−1Y−*x*Ca alloys. The images disclose that the cast alloys contain a dendritic structure confirming non-equilibrium solidification. The presence of some precipitates embedded in the matrix suggests a limited solution of the alloying elements in Mg. The images further show how the precipitates are distributed throughout the microstructure. The micrographs also reveal no significant changes in the microstructure of the alloys after the addition of 0.1% Ca, but the appearance of small amounts of new participates (Point *B* in Fig. 3(b), in gray color) denoted as *A* can be reported. Furthermore, comparing the micrographs suggests that increasing Ca content results in a significant change in the microstructure as well as growth in the dimension and volume fraction of the precipitates (Figs. 3(c) and (d)). In other words, the higher the content of Ca, the more the continuity of the precipitates. In addition, the magnified parts represent the formation of only one type of precipitate in Ca-free alloy (Fig. 3(a)) and two different precipitates with various morphologies in the Ca-bearing alloys (Figs. 3(c) and (d)). One in light color positioned at the grain boundaries as well as the ternary points in the form of bone structure, denoted as *A*, and the other one in gray color with lamellar morphology located at the grain boundaries, denoted as *B*.

Figure 4 represents the typical EDS spectra for the precipitates *A* and *B*, pointed out in Fig. 3(b), and the matrix. Figure 4(a) indicates the presence of three main peaks corresponding to Mg, Zn and Y elements in the precipitates marked as *A* which presents the formation of a ternary intermetallic in all alloys. From the quantitative analysis given Fig. 4, the formation of *I*-phase (Mg_3YZn_6) can be inferred. In contrast, the spectrum and quantitative analysis corresponding to the precipitate *B*, shown in Fig. 4(b), reveal the formation of a different ternary intermetallic phase. Figure 4(c) presents the spectrum of the matrix. The mole fraction presented in Fig. 4(b) implies that the intermetallic $Ca_2Mg_6Zn_3$ is formed. It is believed that the mass ratio of Zn to Y and mole ratio of Zn to Ca are determinants for the formation of intermetallic phases. If the former is higher than 4.38:1, then *I*-phase is precipitated, but if it is between 1.1:1 and 4.38:1, both *I*- and *W*-phases ($Mg_3Zn_3Y_2$) are formed.

On the other hand, if the latter is higher than 1.23:1, then $Ca_2Mg_6Zn_3$ phase is formed, and if it is less than 1.23:1, in addition to $Ca_2Mg_6Zn_3$, more Ca is consumed and Mg_2Ca is formed [33]. Therefore, considering the

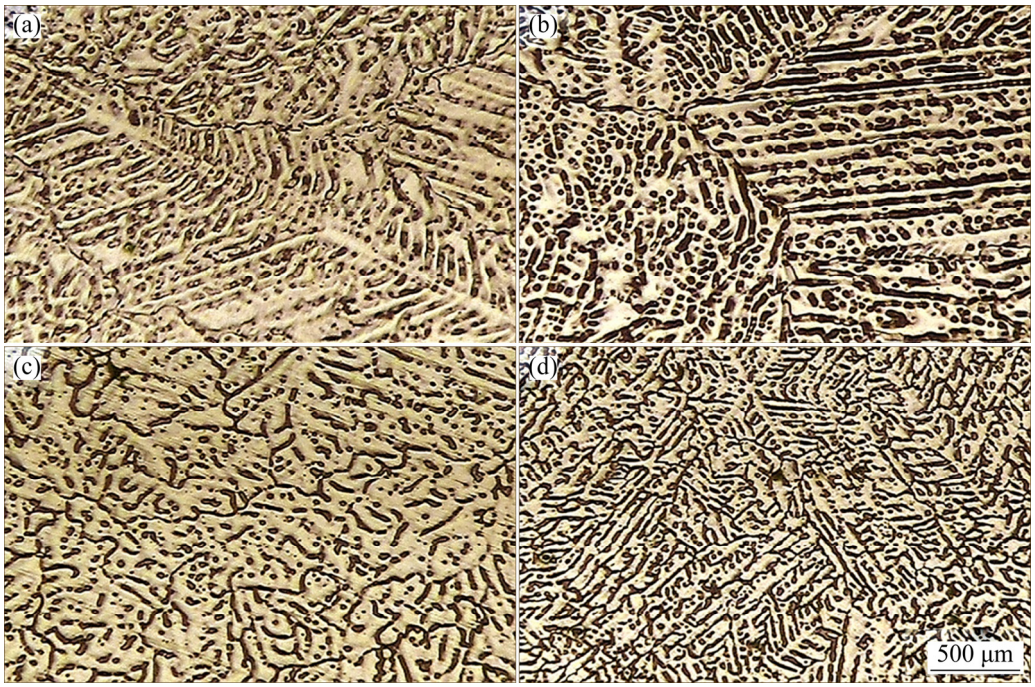

Fig. 2 Typical OM images of as-cast Mg−5Zn−1Y−*x*Ca alloys: (a) *x*=0; (b) *x*=0.1; (c) *x*=0.5; (d) *x*=1.0

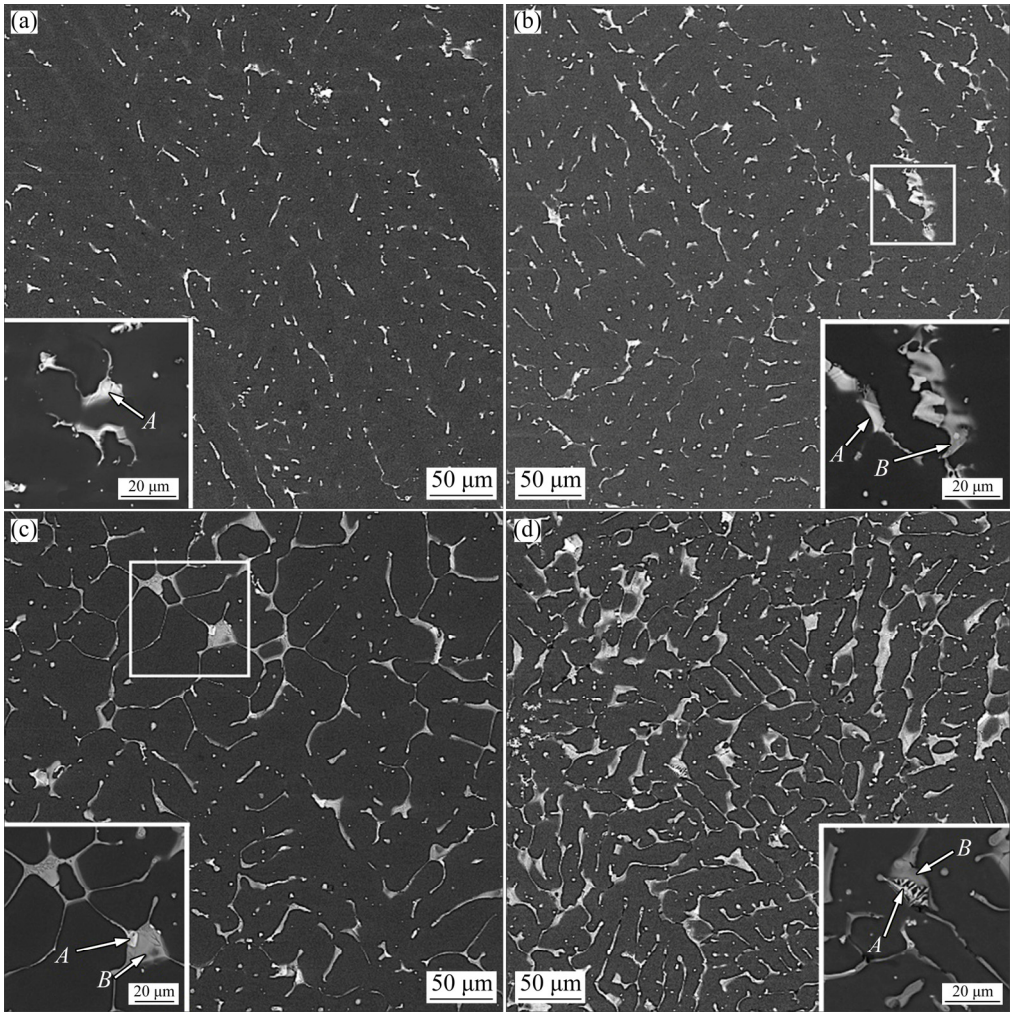

Fig. 3 SEM images of Mg−5Zn−1Y−*x*Ca alloys: (a) *x*=0; (b) *x*=0.1; (c) *x*=0.5; (d) *x*=1.0

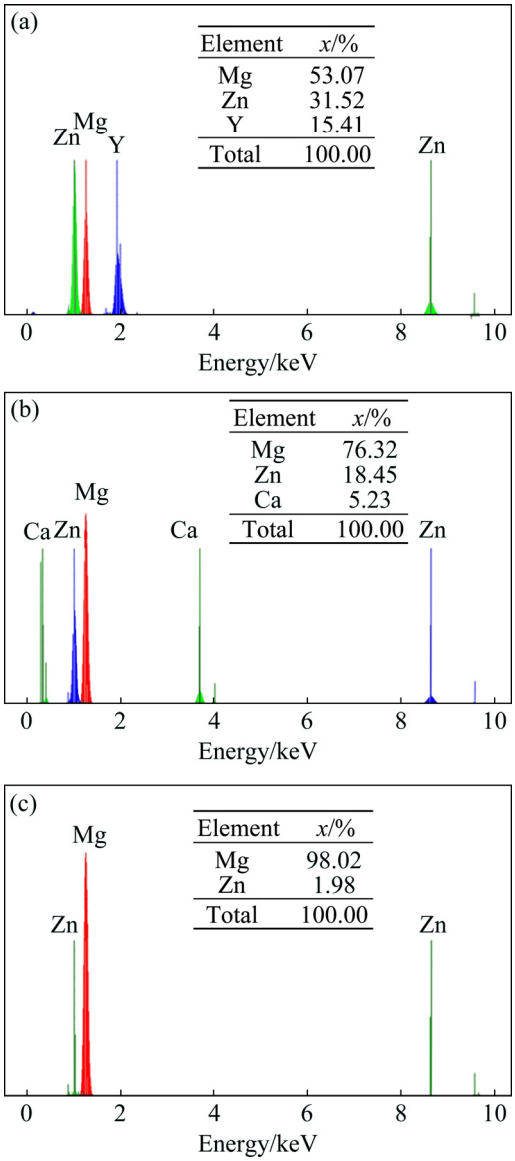

Fig. 4 EDS analysis results of as-cast Mg−5Zn−1Y−0.1Ca alloy: (a) *I*-phase; (b) $Ca_2Mg_6Zn_3$ phase; (c) Matrix

chemical composition of the experimented alloys, the mass ratios of Zn to Y for all alloys are between 5.10:1 and 5.74:1, indicating the formation of just *I*-phase. In contrast, the mole ratios of Zn to Ca for the alloys are in the range of 2.69:1−32.15:1, representing the formation of *I* and $Ca_2Mg_6Zn_3$ phases. The proposed formation of the intermetallics is verified by XRD analysis (Fig. 5) in which the formation of *I*-phase in Mg−5Zn−1Y alloy and both *I* and $Ca_2Mg_6Zn_3$ phases in Mg−5Zn−1Y−Ca alloys are confirmed.

Figure 6 shows the typical optical micrographs of the homogenized alloys. As can be seen, the dendritic structure disappeared in both Ca-free (Fig. 6(a)) and almost in Mg−5Zn−1Y−0.1Ca (Fig. 6(b)) alloys. In addition, compared to the corresponding as-cast alloys (Figs. 2(a) and (b)), the more homogeneous

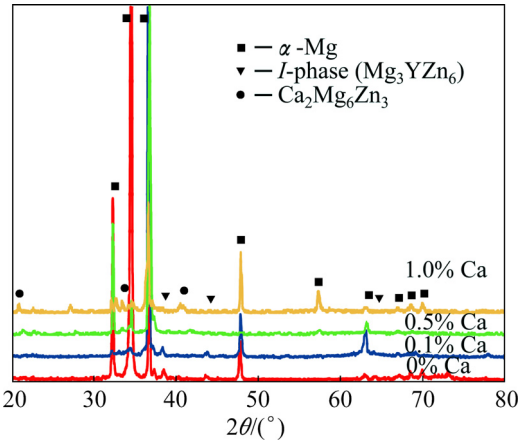

Fig. 5 XRD patters of as-cast Mg−5Zn−1Y−*x*Ca alloys

microstructures with very lower but more globular intermetallics are formed. The structure of other alloys (Figs. 2(c) and (d) is also influenced to some extent, and the continuity of the intermetallics is partly reduced (Figs. 6(c) and (d)).

Figure 7 shows optical micrographs of the extruded alloys at different temperatures. Figures 7(a−c) represent optical micrographs of the extruded Mg−5Zn−1Y alloy at the temperatures of 300, 330, and 370 °C. As can be seen, *I*-phase particles are broken and distributed along the extrusion direction at 300 °C, and DRX simultaneously occurs. At higher temperatures, in addition to modifying the grains, the energy for grain growth was provided and the growth took place.

In other words, the original grains grow, and new grains form, comprising a duality in grain size distribution, called bimodal structure [34]. Looking at the microstructure of this alloy extruded at higher temperatures (Fig. 7(b)), a bimodal structure can be distinguished. This behavior is very pronounced at 370 °C (Fig. 7(c)). It should be noted that with the increase in the temperature of the extrusion, enhanced breaking and elongated intermetallics along the extrusion direction can be observed [35].

Figure 8(a) shows the SEM image from the extruded Mg−5Zn−1Y alloy at 330 °C, representing elongated intermetallic precipitates. The magnified image embedded in Fig. 8(a) highlights an elongated precipitate, denoted as *A*. The quantitative result of EDS analysis presented in Fig. 9(a) further reveals that it is *I*-phase. Figures 7(d−f) show OM images of the extruded Mg−5Zn−1Y−0.1Ca alloy at the temperatures of 300, 330, and 370°C. It is believed that with increasing Ca content a structure with a different nature of dislocation arrangement and plastic behavior is formed [36]. This is apparent because Ca is solved in *α*-Mg matrix partly; consequently, it forms a solid solution which causes the different behaviors of dislocations motion compared with

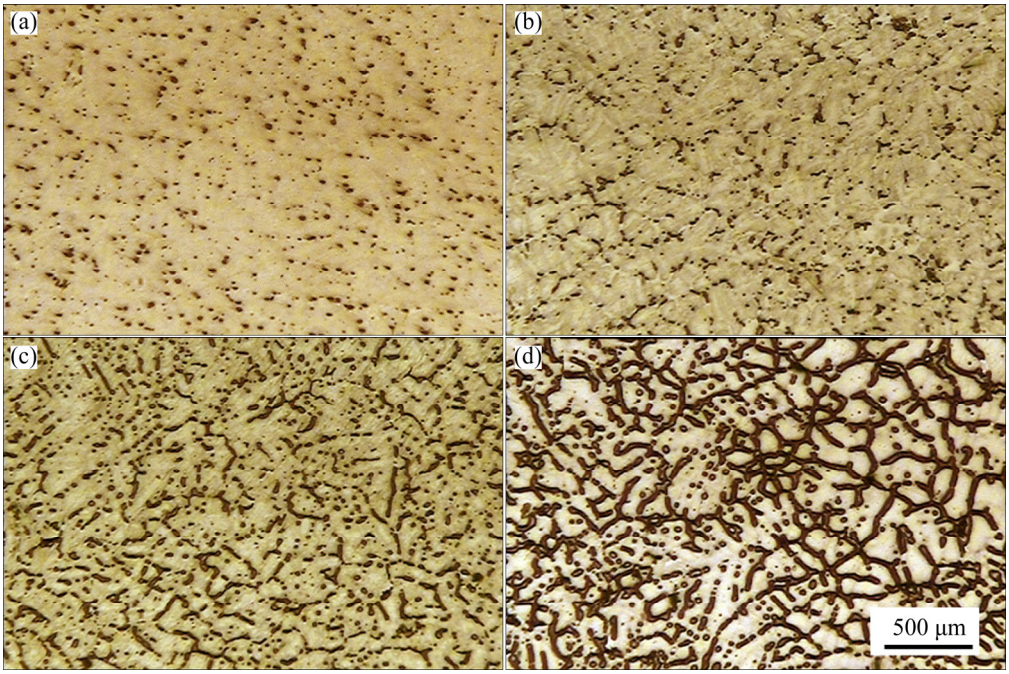

Fig. 6 Optical micrographs of homogenized Mg−5Zn−1Y−*x*Ca alloys: (a) *x*=0; (b) *x*=0.1; (c) *x*=0.5; (d) *x*=1.0

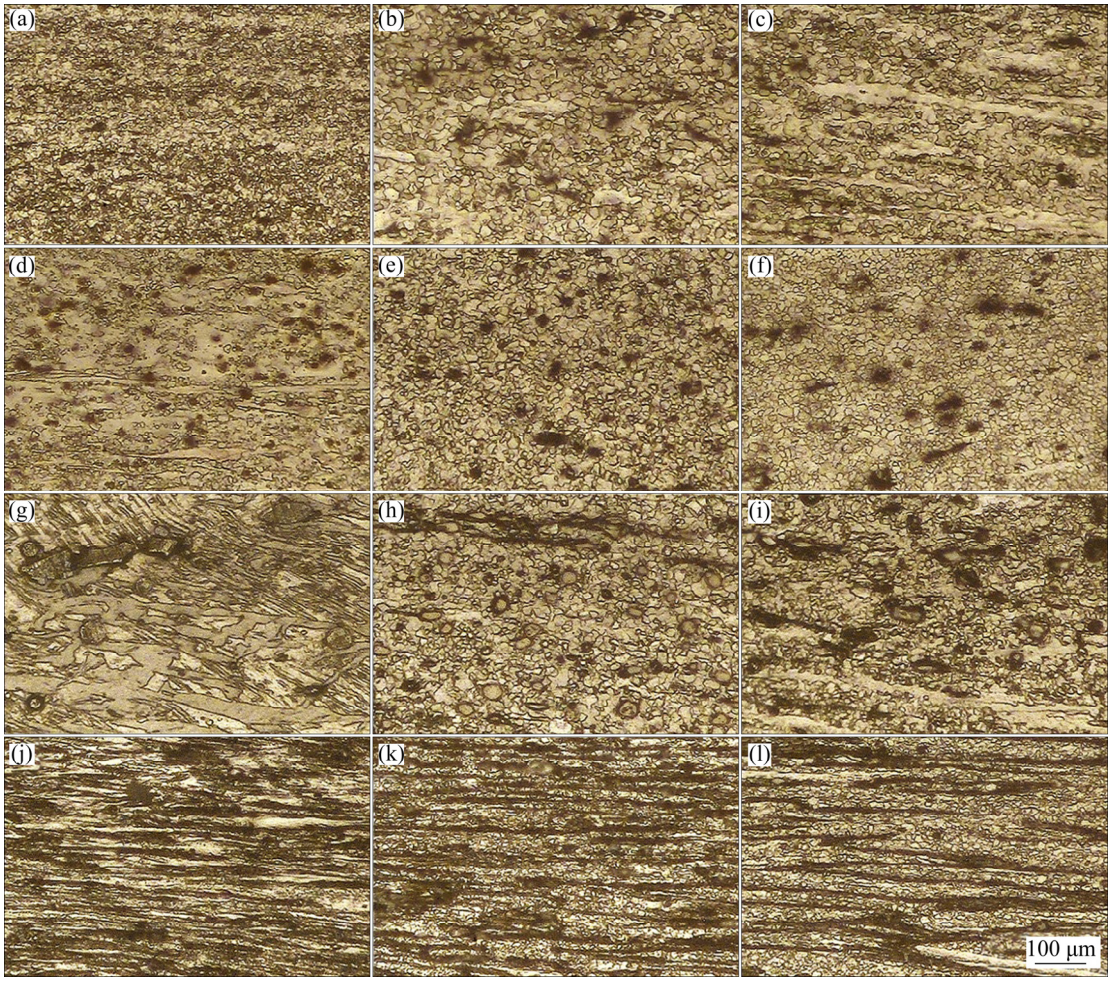

Fig. 7 Optical micrographs of extruded alloys with 0.0% Ca at 300 °C (a), 330 °C (b), and 370 °C (c); with 0.1% Ca at 300 °C (d), 330 °C (e), and 370 °C (f); with 0.5% Ca at 300 °C (g), 330 °C (h), and 370 °C (i); with 1.0% Ca at 300 °C (j), 330 °C (k), and 370 °C (l)

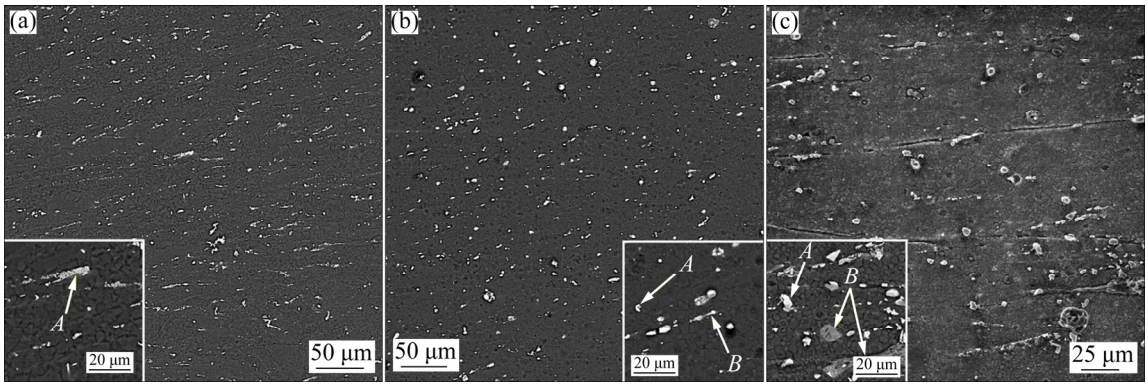

Fig. 8 SEM images of extruded Mg−5Zn−1Y−*x*Ca alloys at 330 °C: (a) *x*=0; (b) *x*=0.1; (c) *x*=0.5

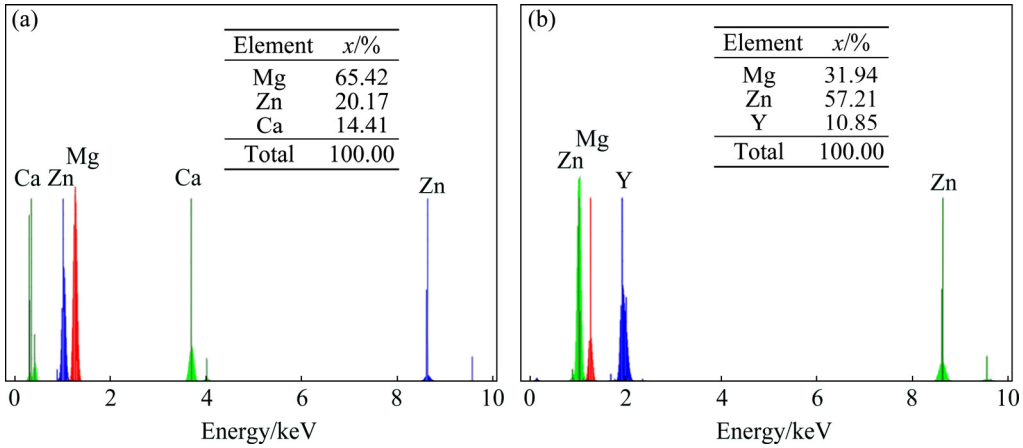

Fig. 9 EDS analysis results of extruded Mg−5Zn−1Y−0.5Ca alloy at 330 °C at point *A* (a) and point *B* (b) marked in Fig. 8

that when the alloy is free of Ca. In other words, the same strain has a different effect in each alloy. On the other hand, the density of dislocations in 0.1% and 0.5% Ca-containing extruded alloys is more definite than that of Ca-free alloy. So, applying the same temperature for producing DRX in the microstructure having a higher density of dislocations is not enough and DRX partially occurs. Therefore, it can most probably be stated that fully DRX occurs with increasing temperature. The increased $Ca_2Mg_6Zn_3$ phase in the microstructure, due to the addition of Ca, and also the breaking and distribution of this intermetallic together with *I*-phase during extrusion process acts as the barriers and further restricts dislocations movement. This causes the dislocations to pile-up at the precipitates resulting in raising the energy of the system and occurrence of DRX to decrease the energy. Completion of DRX trend can be simply observed from Figs. 7(d−f) for Mg−5Zn−1Y−0.1Ca alloy and Figs. 7(g−i) for Mg−5Zn−1Y−0.5Ca alloy with increasing extrusion temperature.

Moreover, it can be remarked that extrusion at 370 °C provides a complete DRX and results in fine and equiaxed grains throughout the microstructure. Figures 8(b) and (c) represent the SEM images of the extruded Mg−5Zn−1Y−0.1Ca and Mg−5Zn−1Y−0.5Ca alloys, respectively, at 330 °C, indicating the presence of elongated *I*-phase and $Ca_2Mg_6Zn_3$ phase. The quantitative EDS result presented in Fig. 9(b) confirms that the precipitates denoted as *B*, are $Ca_2Mg_6Zn_3$ phases. From Fig. 7, it can be seen that the size of the precipitates is higher than 5 μm. It is believed that the interface between such particles and matrix can be appropriate locations for nucleation of DRXed grains [37]. In other words, dislocations are piled-up at the interface and are rearranged to form a DRX nuclei named as particle stimulated nucleation (PSN). Increasing Ca content to 1%, brings about more continuous intermetallics, as can be seen in Figs. 7(j)−(l), and the extrusion force is not able to break them completely into small pieces. Due to more interface area between the intermetallics and matrix in this alloy, the more refined microstructure is formed. Furthermore, as shown in Figs. 7(j)−(l), the alloy extruded at 300 °C contains finer DRX grains (an average of 6.7 μm) compared to that processed at 330 °C (an average of 9.5 μm) and 370 °C (an average of 10 μm). Table 3 provides the grain size of the as-cast and extruded alloys. The sizes also indicate that increasing extrusion

temperature causes the recrystallized grains to grow; however, this behavior is inversely followed by the alloys containing 0.1% and 0.5% Ca, which is attributed to the higher recrystallization temperature for the alloys.

Table 3 Grain size of as-cast and extruded alloys

Alloy	Grain size/μm			
	As-cast	Extruded		
		300 °C	330 °C	370 °C
Mg−5Zn−1Y	792.6	13.6	22.4	31.6
Mg−5Zn−1Y−0.1Ca	731.1	30.4	18.1	10.8
Mg−5Zn−1Y−0.5Ca	449.0	60.2	20.1	13.8
Mg−5Zn−1Y−1Ca	308.7	9.9	11.4	13.6

Figure 10 discloses the SEM images of Mg−5Zn−1Y−1Ca alloy, revealing the elongated and crushed *I*-phase (denoted as *A*) as well as elongated $Ca_2Mg_6Zn_3$ phase (denoted as *B*). As can be seen, after the extrusion process the secondary phase is elongated, resulting in the occurrence of grooves between the matrix and secondary phases, which is due to the removing secondary phases as well as the difference between their elasticity modulus.

3.3 Corrosion behavior of as-cast and extruded alloys

3.3.1 Electrochemical polarization test

Figure 11 shows the polarization curves, corresponding to the as-cast and extruded alloys, obtained from the electrochemical polarization test. The curve similarity suggests the presence of a comparable electrochemical corrosion mechanism in all alloys. It can be clearly found that corrosion potential of the alloys is mainly in a finite range, so corrosion current density of the alloys is required to consider for the evaluation of corrosion behavior. Table 4 lists the electrochemical parameters, including corrosion current density (J_{corr}) and corrosion potential (φ_{corr}), extracted from the curves, as well as corrosion rate (P_i), calculated using Eq. (1). Figure 11 also compares the corrosion rates of the as-cast and extruded alloys. For the Mg−5Zn−1Y alloy (Fig. 11(a)), it can be inferred that extrusion process at 300 °C causes higher corrosion rate. This is attributed to the finer grain size (Figs. 7(a)−(c)) which provides more grain boundaries for the corrosion attack. In other words, as no passive region is present in the polarization curves, the grain boundaries are the initial sites to corrode due to the domination of active corrosion; consequently, the finer the grain size, the more the corrosion rate [8,38]. The grain growth at higher temperatures and formation of the bimodal structure provide fewer grain boundaries to corrode, resulting in an improved corrosion resistance, but not as much as that of the as-cast alloy due to its larger grain size.

With the addition of 0.1% Ca, the corrosion behavior of the extruded alloy compared to that of Ca-free one finds the inverse results. Table 4 indicates that the as-cast Mg−5Zn−1Y−0.1Ca alloy possesses lower corrosion rate compared to the extruded alloy. In other words, the corrosion rate of the as-cast Mg−5Zn−1Y−0.1Ca alloy stands at the lowest level while applying extrusion process causes the corrosion rate of this alloy to increase. This behavior can be described by the microstructures of the as-cast and extruded alloys. The formation of the cathodic particles of $Ca_2Mg_6Zn_3$ [17] at grain boundaries after the addition of 0.1% Ca leads to the development of microgalvanic cells, causing higher corrosion rate of the α-Mg matrix. Furthermore, according to the microstructures of the extruded alloy shown in Figs. 7(d)−(f), DRX occurs partially at 300 °C, but incompletely at 330 °C, while it is completed at 370 °C; thus totally finer and equiaxed grains can be observed. This phenomenon causes increasing grain boundaries with increasing extrusion temperature and due to the domination of active polarization, the corrosion rate of the alloy increases.

In addition, Mg−5Zn−1Y−0.5Ca extruded at 300 °C shows the lowest corrosion rate among the extruded

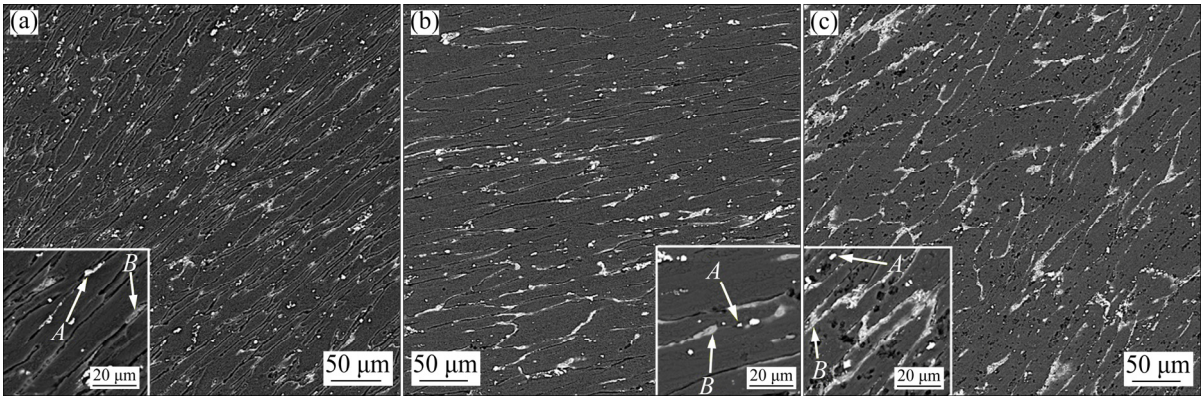

Fig. 10 SEM images of extruded Mg−5Zn−1Y−1Ca alloy at 300 °C (a), 330 °C (b) and 370 °C (c)

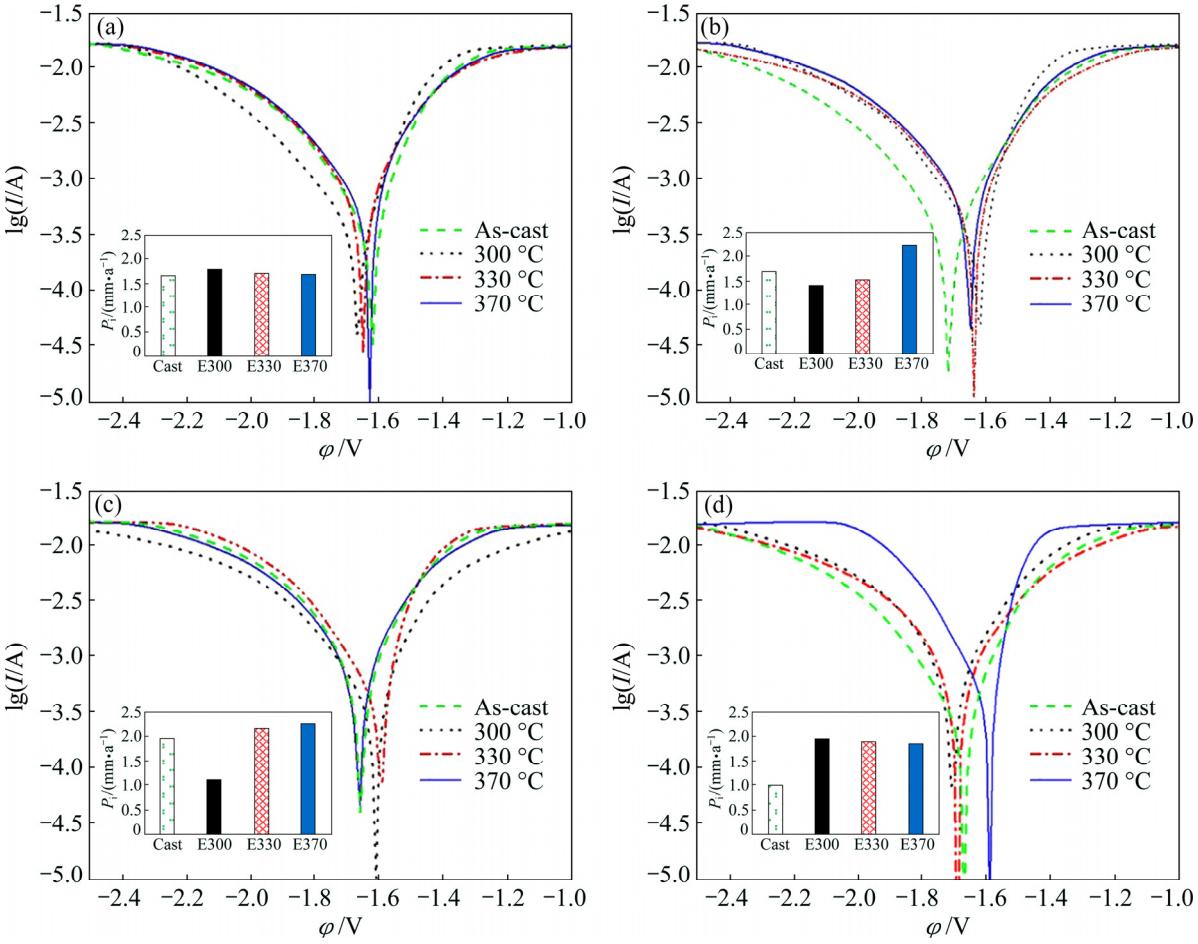

Fig. 11 Polarization curves and corrosion rate chart of alloys with 0.0% (a), 0.1% (b), 0.5% (c), and 1.0% (d) Ca (Cast: As-cast; E300: Extruded at 300 °C; E330: Extruded at 330 °C; E370: Extruded at 370 °C)

Table 4 Electrochemical corrosion parameters of Mg−5Zn−1Y−*x*Ca alloy

Parameter	Alloy condition	Temperature/°C	*x*=0.0%	*x*=0.1%	*x*=0.5%	*x*=1.0%
φ_{corr}/V	As-cast	–	−1.62±0.05	−1.72±0.03	−1.66±0.06	−1.65±0.05
	Extruded	300	−1.66±0.04	−1.62±0.04	−1.61±0.04	−1.70±0.05
		330	−1.72±0.05	−1.64±0.06	−1.59±0.03	−1.69±0.04
		370	−1.63±0.06	−1.65±0.04	−1.66±0.04	−1.59±0.06
J_{corr}/(μA·cm^{-2})	As-cast	–	73.16±2.62	43.98±3.42	86.13±3.28	100.29±3.42
	Extruded	300	77.96±2.80	61.98±2.92	48.59±2.02	85.41±2.87
		330	74.87±2.52	66.67± 2.39	94.66±3.91	82.51±3.14
		370	74.12±2.82	97.84±3.29	99.33±3.07	80.92±3.12
P_i/(mm·a^{-1})	As-cast	–	1.67±0.06	1.00±0.08	1.97±0.07	2.29±0.06
	Extruded	300	1.78±0.06	1.42±0.06	1.11±0.05	1.95±0.07
		330	1.71±0.06	1.52±0.06	2.16±0.09	1.88±0.08
		370	1.69±0.07	2.24±0.07	2.27±0.07	1.85±0.07

alloys. The addition of 0.5% Ca to the alloy causes more intermetallic $Ca_2Mg_6Zn_3$ phase to emerge at grain boundaries resulting in more microcathodic areas and enhancing corrosion rate of the α-Mg matrix. Moreover, the microstructures displayed in Figs. 7(g)−(i) reveal that the Mg−5Zn−1Y−0.5Ca alloy extruded at 300 °C, compared to the alloys extruded at the other temperatures, does not experience the DRX process. Consequently, the coarser grains with fewer grain boundaries form in the alloys extruded at 300 °C; thus corrosion rate is reduced.

On the other hand, increasing temperature causes the formation of a bimodal structure which leads to the increased corrosion rate. So, elevating extrusion temperature brings about higher corrosion rate in this alloy. In contrast, extrusion of Mg−5Zn−1Y−1Ca alloy at the temperature of 300 °C causes a positive influence on the decreasing corrosion rate. This behavior can be described based on the microstructure of the extruded alloy (Figs. 7(j)−(l)). DRXed grains are observed in the alloy extruded at 330 and 370 °C, while a very lower number of grains are remarked in the alloy extruded at 300 °C. Thus, it can be inferred that the lower the grain boundary, the higher the corrosion resistance of the extruded alloy. On the other hand, the intermetallic $Ca_2Mg_6Zn_3$ phase is elongated along the extrusion direction; however, it is not entirely crushed into pieces (Fig. 10). So, the volume of the effective cathode is decreased, resulting in the improvement of corrosion resistance [17].

3.3.2 Immersion test

Mass loss of the as-cast and extruded alloys as a function of Ca content and extrusion temperature are shown in Fig. 12. It can be concluded that two different parameters, i.e., the addition of Ca and extrusion process, compete to influence the corrosion rate. The former in an amount of 0.1% reduces the corrosion rate of the cast alloy for about 7% ((3.80±0.08)−(3.53±0.06) mm/a); however, further increase enhances it. The corrosion rate is calculated to be 20.62 mm/a (around 6 times) when the alloy contains 1% Ca (Fig. 12(d)). In contrast, the latter just improves the corrosion resistance of the alloy containing 1% Ca. In other words, the Mg−5Zn−1Y−1Ca alloy extruded at 300, 330, and 370 °C shows 8.24%, 66.16%, and 73.42% reduction in the corrosion rate, respectively. It should be noted that the corrosion rate of the extruded alloy is still more than that of the as-cast alloy containing up to 0.5% Ca.

Moreover, the Mg−5Zn−1Y−0.5Ca alloy extruded at 300 °C shows the lowest corrosion rate ((2.86±0.05) mm/a) among the extruded alloys. The above findings highly support the electrochemical polarization outcomes, indicating conclusive results. The above different results obtained from the extruded alloys at different extrusion temperatures are originated from the microstructure evolution during the extrusion process as discussed in Section 3.3.1.

Figure 13 shows some typical SEM images of the corroded surfaces as well as corrosion products of two

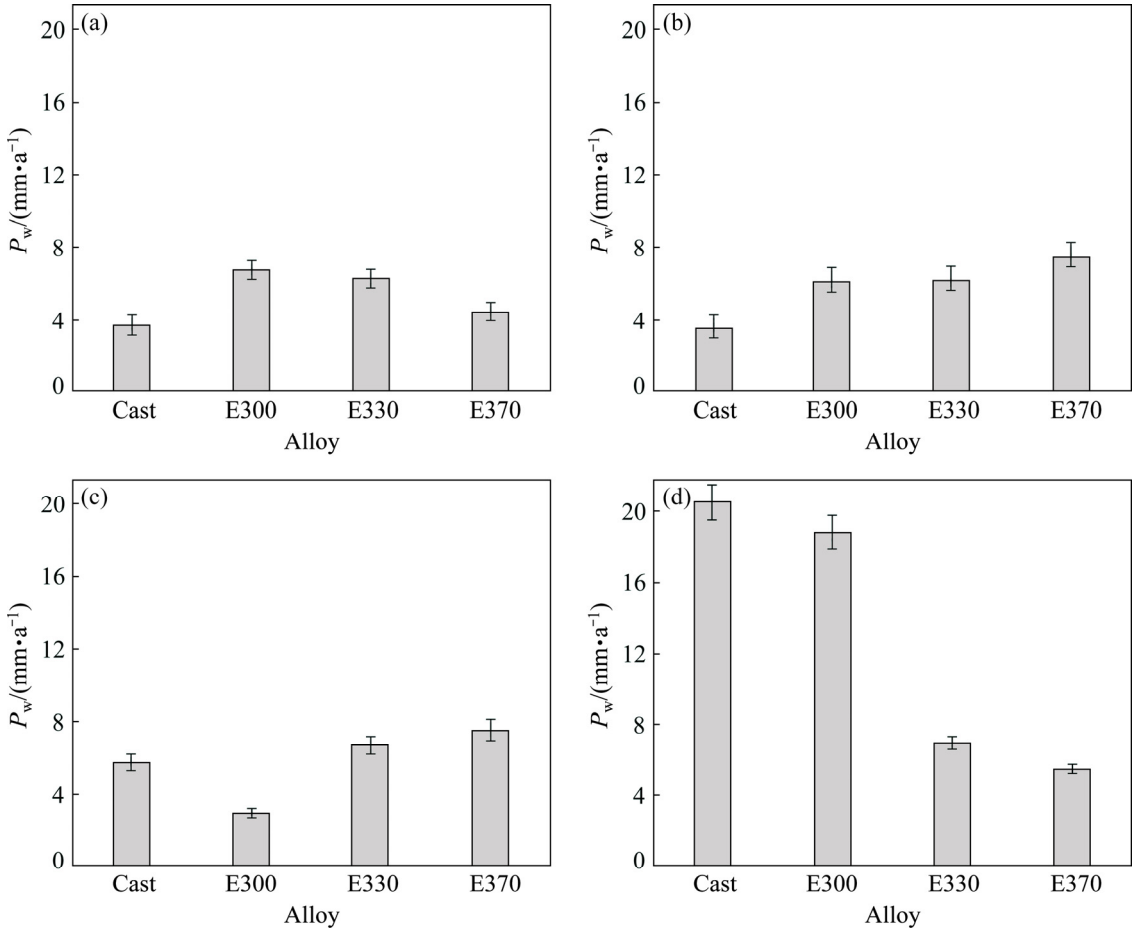

Fig. 12 Mass loss of as-cast and extruded alloys with different Ca contents at different temperatures: (a) 0.0%; (b) 0.1%; (c) 0.5%; (d) 1.0%

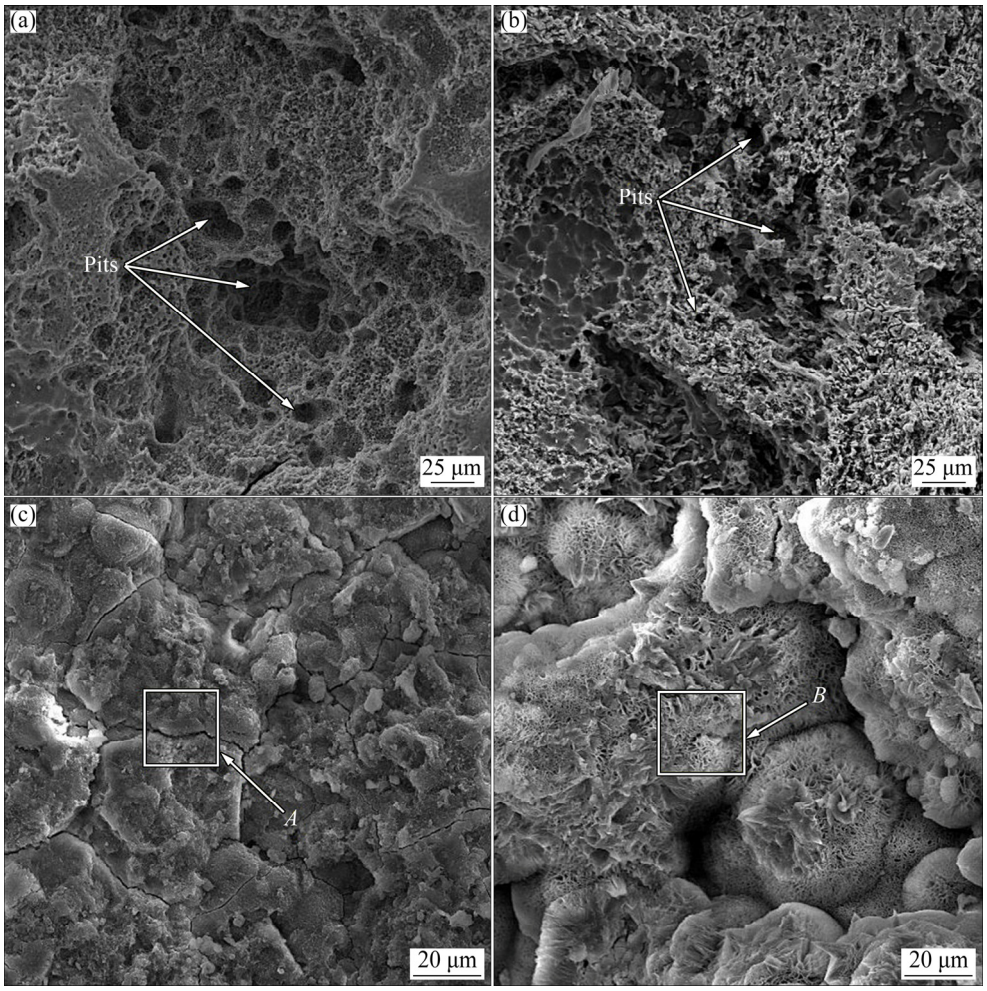

Fig. 13 SEM images of corroded surfaces (a, b) and corrosion products (c, d) of Mg−5Zn−1Y (a, c) and Mg−5Zn−1Y−1Ca (b, d) alloys extruded at 330 °C, respectively

Mg−5Zn−1Y and Mg−5Zn−1Y−1Ca alloys extruded at 330 °C after immersion test. In addition to the uniform corrosion of the alloy, Fig. 13(a) clearly discloses the presence of a number of pits accumulated on the corroded surface of the Mg−5Zn−1Y alloy. The formation of such pits is attributed to the corrosion of *I*-phase, due to its more negative electrochemical potential in comparison to the α-Mg matrix in SBF [22], through the development of microgalvanic cells between α-Mg matrix as the cathode, and *I*-phase as the anode. Figure 13(b) shows the SEM image of the surface of the Mg−5Zn−1Y−1Ca alloy extruded at 330 °C after being corroded in SBF throughout immersion test. It is seen that the surface of the alloy is strongly corroded and, the level of corrosion is more pronounced compared to the Ca-free alloy shown in Fig. 13(a).

This is because of the Ca addition which forms microcathodic sites of $Ca_2Mg_6Zn_3$ compared to the α-Mg matrix and enhances the corrosion rate. In addition, as mentioned above, *I*-phase microanodic sites are corroded to form pits, simultaneously. Figures 13(c) and (d) demonstrate the corrosion products formed on both extruded alloys at 330 °C, Mg−5Zn−1Y, and Mg−5Zn−1Y−1Ca, respectively, after the immersion test.

Figure 14 illustrates the EDS analyses of two points and the corresponding quantitative data for the corrosion products formed on the surface of the alloys discussed in Fig. 13. The mole ratio of Mg to O in the corrosion products formed on Mg−5Zn−1Y alloy (Fig. 14(a)), as well as the presence of Mg, Ca, P, and O in the corrosion products formed on Mg−5Zn−1Y−1Ca alloy (Fig. 14(a)), suggest that the corrosion products are mainly composed of $Mg(OH)_2$ and calcium phosphate compound, respectively. The quantitative analysis shown in Fig. 14(b) proposes Ca/P mole ratio of 1.07:1, which is below the stoichiometric hydroxyapatite (HA, 1.67:1), indicating the formation of Ca-deficit hydroxyapatite. In other words, Ca is substituted by Mg ion in the HA lattice [39]. It can be seen from Fig. 14(b), more amount of HA is estimated, indicating Ca addition enhances the biodegradation of alloy.

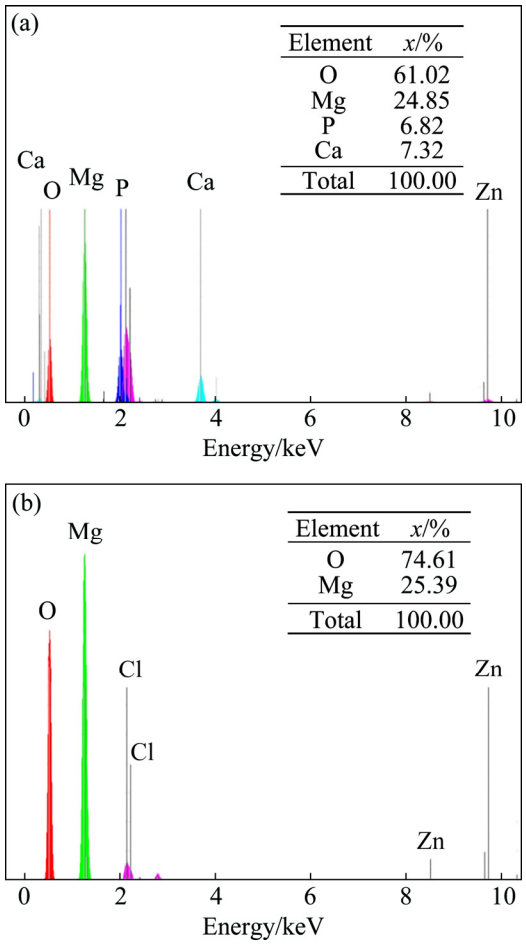

Fig. 14 EDS analysis results taken from corrosion products formed on surface of Mg−5Zn−1Y (a) and Mg−5Zn−1Y−1Ca (b) alloys

4 Conclusions

1) Microscopic examinations showed that Mg−5Zn−1Y alloy is composed of the α-Mg matrix and intermetallic Mg_3YZn_6. Ca addition causes lamellar intermetallic $Ca_2Mg_6Zn_3$ to form mostly at grain boundaries; the more the Ca content, the more the $Ca_2Mg_6Zn_3$.

2) The addition of Ca to Mg−5Zn−1Y alloy refined the corresponding microstructure and higher amount of Ca content led to the more refined microstructure. The domination of active polarization in Mg−5Zn−1Y−xCa alloy in SBF resulted in the higher corrosion rate in Mg−5Zn−1Y−1Ca alloy.

3) The more intermetallic $Ca_2Mg_6Zn_3$ phase, as well as the more refined microstructure, led to the higher biodegradation rate of Mg−5Zn−1Y−1Ca alloy among all the as-cast alloys in SBF.

4) Mg−5Zn−1Y−0.5Ca alloy extruded at 300 °C showed lower biodegradation rate than other alloys due to the absence of DRX grains and presence of larger grains.

5) Corrosion resistance of the Ca-free and 1% Ca-bearing alloys was improved with increasing extrusion temperature, although the corrosion rate of the extruded Ca-free alloy, due to its larger grain size and lower volume of the effective secondary phases cathode, was still higher than that of the as-cast one.

Acknowledgments

The authors acknowledge Shahid Rajaee Teacher Training University for the financial support (Vote No. 26234) and providing research facilities.

References

[1] ESLAMI HARANDI S, IDRIS M H, JAFARI H. Effect of forging process on microstructure, mechanical and corrosion properties of biodegradable Mg−1Ca alloy [J]. Materials and Design, 2011, 32: 2596−2603.

[2] JIANG Hong-feng, WANG Jing-bo, CHEN Min-fang, LIU De-bao. Biological activity evaluation of magnesium fluoride coated Mg−Zn−Zr alloy in vivo [J]. Materials Science and Engineering C, 2017, 75: 1068−1074.

[3] RICHARDSON H, MARADZE D, LYONS S, ZHENG Yu-feng, LIU Yang. Corrosion of magnesium and magnesium–calcium alloy in biologically-simulated environment [J]. Progress in Natural Science: Materials International, 2014, 24: 539−546.

[4] QIN Feng-xiang, XIE Guo-qiang. DAN Zhen-hua, ZHU Sheng-li, SEKI I. Corrosion behavior and mechanical properties of Mg−Zn−Ca amorphous alloys [J]. Intermetallics, 2013, 42: 9−13.

[5] PERSAUD-SHARMA D, MCGORON A. Biodegradable magnesium alloys: A review of material development and applications [J]. Journal of Biomimetics, Biomaterials and Tissue Engineering, 2012, 3: 25−39.

[6] POINERN G E J, BRUNDAVANAM S, FAWCETT D. Biomedical magnesium alloys: A review of material properties, surface modifications and potential as a biodegradable orthopaedic implant [J]. American Journal of Biomedical Engineering, 2012, 2: 218−240.

[7] ESLAMI HARANDI S, MIRSHAHI M, KOLEINI S I M H, JAFARI H, ABDUL KADIR M R. Effect of calcium content on the microstructure, hardness and in-vitro corrosion behavior of biodegradable Mg−Ca binary alloy [J]. Materials Research, 2013, 16: 11−18.

[8] GHAFFARI SHAHRI S M, IDRIS M H, JAFARI H, GHOLAMPOUR B, ASSADIAN M. Effect of solution treatment on corrosion characteristics of the biodegradable Mg−6Zn alloy [J]. Transactions of Nonferrous Metals Society of China, 2015, 25: 1490−1499.

[9] KOLEINI S, IDRIS M H, JAFARI H. Influence of hot rolling parameters on microstructure and biodegradability of Mg−1Ca alloy in simulated body fluid [J]. Materials and Design, 2012, 33: 20−25.

[10] LI Hua-fang, ZHENG Yu-eng, QIN Ling. Progress of biodegradable metals [J]. Progress in Natural Science: Materials International, 2014, 24: 414−422.

[11] CUI Lan-yue, XU Ji, LU Na, ZENG Rong-chang, ZOU Yu-hong, LI Shuo-qi, ZHANG Fen. In vitro corrosion resistance and antibacterial properties of layer-by-layer assembled chitosan/poly-L-glutamic acid

coating on AZ31 magnesium alloys [J]. Transactions of Nonferrous Metals Society of China, 2017, 27: 1081−1086.

[12] ZHOU Peng, GONG Hao-ran. Phase Stability, mechanical property, and electronic structure of an Mg−Ca system [J]. Journal of the Mechanical Behavior of Biomedical Materials, 2012, 8: 154−164.

[13] XU Zhi-gang, SMITH C, CHEN Shuo, SANKAR J. Development and microstructural characterization of Mg−Zn−Ca alloys for biomedical applications [J]. Materials Science and Engineering B, 2011, 176: 1660−1665.

[14] LI Nan, ZHENG Yu-feng, Novel magnesium alloys developed for biomedical application: A review [J]. Journal of Materials Science & Technology, 2013, 29: 489−502.

[15] QIN Feng-xiang, XIE Guo-qiang, DAN Zhen-hua, ZHU Sheng-li, SEKI I. Corrosion behavior and mechanical properties of Mg−Zn−Ca amorphous alloys [J]. Intermetallics, 2013, 42: 9−13.

[16] ZHANG Bao-ping, HOU Yun-long, WANG Xiao-dan, WANG Yin, GENG Lin. Mechanical properties, degradation performance and cytotoxicity of Mg−Zn−Ca biomedical alloys with different compositions [J]. Materials Science and Engineering C, 2011, 31: 1667−1673.

[17] TONG Li-bo, ZHENG Ming-yi, XU Shi-wei, HU Xiao-shi, WU Kun, KAMADO S, WANG Guo-jun, LV Xin-yu. Room temperature compressive deformation behavior of Mg−Zn−Ca alloy processed by equal channel angular pressing [J]. Materials Science and Engineering A, 2010, 528: 672−679.

[18] SINGH L K, SRINIVASAN A, PILLAI U T S, JOSEPH M A, PAI B C. The effect of yttrium addition on the microstructure and mechanical properties of Mg alloys [J]. Transactions of Indian Institute of Metals, 2015, 68: 331−339.

[19] SUN Hong-fei, LI Cheng-jie, FANG Wen-bin. Evolution of microstructure and mechanical properties of Mg−3.0Zn−0.2Ca−0.5Y alloy by extrusion at various temperatures [J]. Journal of Materials Processing Technology, 2015, 229: 633−640.

[20] WU Luo-yi, LI Hao-tian, YANG Zhong. Microstructure evolution during heat treatment of Mg–Gd–Y–Zn–Zr alloy and its low-cycle fatigue behavior at 573 K [J]. Transactions of Nonferrous Metals Society of China, 2017, 27: 1026−1035.

[21] JAFARI H, RAHIMI F, SHEKHSOFLA Z. In vitro corrosion behavior of Mg−5Zn alloy containing low Y contents [J]. Materials Corrosion, 2016, 67: 396−405.

[22] KAINER K U. Magnesium: Alloys and technology [M]. Germany: Wiley-VCH, 2003.

[23] HAN Bing-qiang, DUNAND D C. Creep of magnesium strengthened with high volume fractions of yttria dispersoids [J]. Materials Science and Engineering A, 2001, 300: 235−244.

[24] ZHANG Kui, ZHANG Xin, DENG Xia, LI Xing-gang, MA Ming-long. Relationship between extrusion, Y and corrosion behavior of Mg−Y alloy in NaCl aqueous solution [J]. Journal of Magnesium Alloys, 2013, 1: 134−138.

[25] ZENG Rong-chang, QI Wei-chen, CUI Hong-zhi, ZHANG Fen, LI Shuo-qi, HAN En-hou. In vitro corrosion of as-extruded Mg−Ca alloys—The influence of Ca concentration [J]. Corrosion Science, 2015, 96: 23–31.

[26] HOU Li-da, LI Zhen, ZHAO Hong, PAN Yu, PAVLINICH S, LIU Xi-wei, LI Xin-lin, ZHENG Yu-feng, LI Li. Microstructure, mechanical properties, corrosion behavior and biocompatibility of as-extruded biodegradable Mg−3Sn−1Zn−0.5Mn alloy [J]. Journal of Materials Science and Technology, 2016, 32: 874−882.

[27] GUI Zhen-zhen, KANG Kang, LI Yuan-yuan. Mechanical and corrosion properties of Mg−Gd−Zn−Zr−Mn biodegradable alloy by hot extrusion [J]. Journal of Alloys and Compounds, 2016, 685: 222−230.

[28] BEAK Soo-Min, KIM Hyeon-Ju, JEONG Hu-Young, SOHN So-Dam, SHIN Hyung-Joon, CHOI Kyung-Jin, LEE Ki-Suk, LEE Jung-Gu, YIM Chang-Dong, YOU Bong-Sun, HA Heon-Young, PARK Sung-Soo. Effect of alloyed Ca on the microstructure and corrosion properties of extruded AZ61 Mg alloy [J]. Corrosion Science, 2016, 112: 44−53.

[29] TONG Li-bo, ZHANG Qing-xin, JIANG Zhong-hao, ZHANG Jun-bao, MENG Jian, CHENG L R, ZHANG Hong-jie. Microstructures, mechanical properties and corrosion resistances of extruded Mg−Zn−Ca−*x*Ce/La alloys [J]. Journal of the Mechanical Behavior of Biomedical Materials, 2016, 62: 57−70.

[30] WANG Li-qing, QIN Gao-wu, SUN Shi-neng, REN Yu-ping, LI Song. Effect of solid solution treatment on in vitro degradation rate of as-extruded Mg−Zn−Ag alloys [J]. Transactions of Nonferrous Metals Society of China, 2017, 27: 2607−2612.

[31] LEE Y C, DAHLE A K, STJOHN D H. The role of solute in grain refinement of magnesium [J]. Metallurgical and Materials Transactions A, 2000, 31: 2895−2906.

[32] ZHANG Er-lin, YANG Lei. Microstructure, mechanical properties and bio-corrosion properties of Mg−Zn−Mn−Ca alloy for biomedical application [J]. Materials Science and Engineering A, 2008, 497: 111−118.

[33] YANG Ming-bo, WU De-yong, HOU Meng-dan, PAN Fu-sheng. As-cast microstructures and mechanical properties ofMg−4Zn−*x*Y−1Ca (*x*=1.0, 1.5, 2.0, 3.0) magnesium alloys [J]. Transactions of Nonferrous Metals Society of China, 2015, 25: 721−731.

[34] ZHOU Xiao-jie, LIU Chu-ming, GAO Yong-hao, JIANG Shu-nong, LIU Wen-hui, LU Li-wei. Microstructure and mechanical properties of extruded Mg−Gd−Y−Zn−Zr alloys filled with intragranular LPSO phases [J]. Materials Characterization, 2018, 135: 76−83.

[35] ZHU Shao-zhen, LUO Tian-jiao, ZHANG Ting-an, LIU Yun-teng, YANG Yuan-sheng. Effects of extrusion and heat treatments on microstructure and mechanical properties of Mg−8Zn−1Al−0.5Cu−0.5Mn alloy [J]. Transactions of Nonferrous Metals Society of China, 2017, 27: 73−81.

[36] VOGEL M, KRAFT O, ARZT E. Effect of calcium additions on the creep behavior of magnesium die-cast alloy ZA85 [J]. Metallurgical and Materials Transactions A, 2005, 36: 1713−1719.

[37] RAMESH C S, KESHAVAMURTHY R, KOPPAD P G, KASHYAP K T. Role of particle stimulated nucleation in recrystallization of hot extruded Al 6061/SiCp composites [J]. Transactions of Nonferrous Metals Society of China, 2013, 23: 53−58.

[38] SONG Guang-ling, XU Zhen-qing. The surface, microstructure and corrosion of magnesium alloy AZ31 sheet [J]. Electrochimica Acta, 2010, 55: 4148−4161.

[39] ŠUPOVÁ M. Substituted hydroxyapatites for biomedical applications: A review [J]. Ceramics International, 2015, 41: 9203−9231.

Mg−5Zn−1Y−*x*Ca 合金的显微组织表征及挤压温度对其生物降解行为的影响

F. DOOST MOHAMMADI, H. JAFARI

Materials Engineering Department, Faculty of Materials Engineering and Modern Technologies, Shahid Rajaee Teacher Training University, 16785-136 Tehran, Iran

摘　要：研究不同钙含量 (0.0%、0.1%、0.5%和 1.0%，质量分数)的铸态和热挤压态 Mg−5Zn−1Y 合金的显微组织和生物降解行为，挤压温度分别为 300、330 和 370 °C。研究合金的化学成分、相组成、显微组织和生物降解行为。宏观和微观检测表明，钙的加入细化了晶粒结构，形成了金属间化合物相 $Ca_2Mg_6Zn_3$。热挤压过程使金属间化合物相破碎为细小颗粒，并沿挤压方向分布。而且，几乎所有的合金中都发生了动态再结晶，且在 370 °C 挤压的合金中形成了更多的双态组织。极化曲线显示无钝化区，表明活性极化在合金中占主导地位，因此，通过添加钙使晶粒细化和通过热挤压发生动态再结晶会增加合金的生物降解速率。研究结果表明，铸态 Mg−5Zn−1Y−0.1Ca 合金的耐腐蚀性最好，而在挤压态合金中，300 °C 挤压的 Mg−5Zn−1Y−0.5Ca 合金表现出最低的生物降解速率。因此，热挤压并非总是能改善镁合金的生物降解行为。

关键词：镁合金；挤压温度；生物降解；再结晶；双态组织

(Edited by Xiang-qun LI)